The Phase Evolution and Lattice Dynamics of Dy^{3+}/Sr^{2+} Co-Doped KNN Ferroelectric Ceramics

JianFeng Wu(吴剑锋)[1] , ZheTing Zhang(张哲艇)[2] , Kai Jiang(姜凯)[2*] , LiBing Chen(陈立冰)[1] , Jun Wang(王军)[1§] and Kai Dai(戴凯)[1†]

[1] *College of Science, Shanghai Institute of Technology, Shanghai 201418, China*

[2] *School of Integrated Circuits, Shanghai Dianji University, Shanghai 200240, China*

†Corresponding author. E-mail: daikai@sit.edu.cn

§Corresponding author. E-mail: wangj@sit.edu.cn

* Corresponding author. E-mail: 32077@sdju.edu.cn

Abstract

The phase structure serves as the fundamental determinant of the macroscopic optoelectronic response in ferroelectric ceramics, and therefore its evolutionary behavior constitutes the physical basis for understanding the functional properties. In this work, Dy^{3+}/Sr^{2+} co-doped $(K_{0.5}Na_{0.5})NbO_3$ ceramics are comprehensively investigated via condensed matter spectroscopy. Doping-induced ionic radius mismatch produces lattice distortion, tunes A-site cation ordering, and promotes O–T phase coexistence at room temperature, while inducing composition-dependent evolution of the optical band gap and luminescence properties. Temperature-dependent Raman and PL spectra confirm successive phase transitions and nonlinear thermal drift of luminescence and Raman peaks governed by electron-phonon coupling. A composition-temperature phase diagram was built to verify that doping modulates phase transition temperatures, yielding optimal optical properties and relaxor ferroelectric features. These findings elucidate the mutual coupling among lattice symmetry, electronic structure, and optoelectronic properties, providing theoretical guidance for the design of high-performance lead-free ferroelectric ceramics.

Keywords: Lead-free ferroelectric ceramics, rare-earth ion doping, Phonon dynamics, Phase transition

PACS: 77.84.Ek, 77.80.B-，63.20.-e

1.Introduction

†Corresponding author. E-mail: daikai@sit.edu.cn

The continuous growth of global energy consumption has raised higher requirements for high-performance and eco-friendly optoelectronic functional materials.[1] Lead-free ferroelectric ceramics possess superior multifunctional optoelectronic properties, excellent thermal stability, and environmental compatibility, making them ideal candidates for energy conversion and optoelectronic devices.[2-5] Among them, potassium sodium niobate (KNN)-based lead-free ceramics exhibit remarkable performance tunability and wide application adaptability, showing great potential for multifunctional optoelectronic applications.[6-8] Nevertheless, the practical engineering applications of conventional KNN-based ceramics are still restricted by several bottlenecks.[1] The ambiguous doping modulation mechanisms and complex structure–performance relationships hinder the precise regulation of optical properties and limit the design reliability and operational stability of optoelectronic devices, thereby restricting their widespread applications in high-end optoelectronic fields.[9-12]

Existing studies have demonstrated that A-site multi-ion substitution can effectively tailor the phase structure and intrinsic optoelectronic properties of KNN systems. This enhancement strategy promotes the transformation of long-range ordered ferroelectric domains into diffuse polar nanoregions (PNRs), which suppresses light scattering and improves optical transparency, while optimizing luminescence efficiency through crystal field modulation.[13-18] Furthermore, rare-earth ion doping endows KNN ceramics with prominent photoluminescence characteristics, realizing the multifunctional coupling of luminescence, ferroelectricity, and piezoelectricity, and providing an effective approach for the construction of high-performance integrated optoelectronic materials.[12,19-25] Huang et al. achieved significant optoelectronic performance through the co-doping design of Dy^{3+}/Sr^{2+}, with a visible light transmittance exceeding 50%, demonstrating the distinct advantages of A-site multi-ion co-doping modification.[26] However, current relevant

§Corresponding author. E-mail: wangj@sit.edu.cn
* Corresponding author. E-mail: 32077@sdju.edu.cn

researches still have obvious research gaps on the phase structure regulation mechanism of rare-earth co-modified KNN ceramics.

The optoelectronic properties of materials are essentially determined by their microscopic structures, where the evolution of structures dominates the modulation of performances. It has been confirmed that the room-temperature multiphase coexistence structure is critical for achieving excellent optoelectronic and piezoelectric properties in KNN-based ceramics.[27-29] Ferroelectric materials undergo complex structural phase transitions under external stimuli such as temperature, electric field, and light irradiation. These transitions induce synchronous variations in dielectric response, lattice dynamics, and local crystal field environments, ultimately determining core optoelectronic parameters including optical band gap, luminescence efficiency, and optical transparency.[30-32] Among various external fields, temperature serves as a fundamental and core parameter for regulating the phase transition and microstructural evolution of KNN-based ceramics. The KNN-based ceramics undergo successive orthorhombic–tetragonal-cubic (O→T→C) phase transitions with increasing temperature.[33-34] The thermodynamic stability range and transition path of each phase directly govern the service temperature range and performance stability of the materials. Therefore, establishing accurate phase diagrams and revealing temperature-induced phase evolution are essential for clarifying the performance regulation mechanism. Advanced condensed matter spectroscopy techniques enable precise characterization of phase transition processes and microstructural evolution, serving as powerful tools for elucidating the structure-performance relationship.[35] Accordingly, in-depth investigation of the structural evolution and the coupling mechanism between lattice dynamics and electronic band structures is of great significance for revealing the intrinsic physical mechanism of the superior optoelectronic performances.

To tackle the aforementioned unsolved scientific questions, we fabricated a set of KNN-based ferroelectric ceramics through the conventional solid-state reaction method. Multiple complementary characterization techniques, including X-ray diffraction (XRD) Rietveld refinement, temperature-dependent Raman spectroscopy,

photoluminescence (PL) spectroscopy and spectroscopic ellipsometry, were employed to systematically decode how A-site dopants modulate lattice distortion, lattice phonon dynamics, local crystal-field surroundings and intrinsic electronic band structures. Sequential structural phase transitions were clearly identified from abnormal phonon responses and nonlinear PL peak shifts originating from electron–phonon coupling; meanwhile, a complete composition–temperature phase diagram of this co-doped system was quantitatively established. This work deepens fundamental understanding of the reciprocal coupling between lattice vibration, electronic configuration and luminescence emission in rare-earth modified KNN perovskites, providing a spectroscopic blueprint to design high-performance lead-free ferroelectric ceramics with customizable multifunctional features.

2.Materials and methods

$(K_{0.5}Na_{0.5})_{0.95-0.01x}Dy_{0.01x}Sr_{0.05}NbO_3$ (denoted as *x*Dy–5Sr–KNN, with *x*=0.25,0.5,0.75,1) ceramics were prepared by the conventional solid-state reaction.[26] Analytical-grade Dy_2O_3 (99.99%), $SrCO_3$ (99.9%), Na_2CO_3(99.99%), K_2CO_3 (99.99%), and Nb_2O_5 (99.9%) were used as raw materials. The stoichiometric powders were ball-milled with ZrO_2 balls and anhydrous ethanol for 12 h and subsequently calcined at 850° C for 4 h. The calcined powders were further ball-milled for 12 h to achieve homogeneous mixing. A binder of 6 wt% polyvinyl alcohol (PVA) was added, and the mixture was pressed into thin disks with a diameter of approximately 10 mm and a thickness of 1 mm under a pressure of 300 MPa. The green pressing was heated at 800°C for 2 h to completely decompose and remove the PVA, followed by sintering at 1160°C for 6 h. The as-sintered ceramics were thinned and polished to a final thickness of 0.35 mm for optical characterizations.

The vibrational behavior and photoluminescence properties of the *x*Dy–5Sr–KNN ceramics were systematically characterized by a micro-Raman spectrometer equipped with an ultralow frequency accessory (Jobin-Yvon LabRAM HR Evolution, Horiba), covering the spectral range from 50 to 950 cm^{-1} and 630–690 nm with a 532 nm laser as the excitation source. Temperature-dependent Raman scattering and PL Spectra

were obtained over the range of 200 to 800 K utilizing a Linkam THMSE 600 heating/cooling platform. The temperature effects were calibrated according to the Bose-Einstein distribution equation[36]: $n(\omega, T) = [\exp(\hbar\omega/kT)-1]^{-1}$, where $\hbar$ represents the reduced Planck constant, ω denotes the phonon wave number, k is the Boltzmann constant, and T indicates the temperature. The optical transition properties in the range of 250 to 600 nm were investigated by the ultraviolet-visible spectroscopic ellipsometer (V-VASE, J.A. Woolam Co., Inc.) at a fixed incidence angle of 70°, while the data were analyzed using the WVASE32 software package. The phase structures of the *x*Dy–5Sr–KNN ceramics were characterized by X-ray diffraction (XRD, Rigaku SmartLab SE) equipped with Cu Kα radiation (λ = 1.5406 Å), while the phase identification was performed by comparing the experimental data with standard PDF cards and Rietveld refinement.

3.Results and discussion

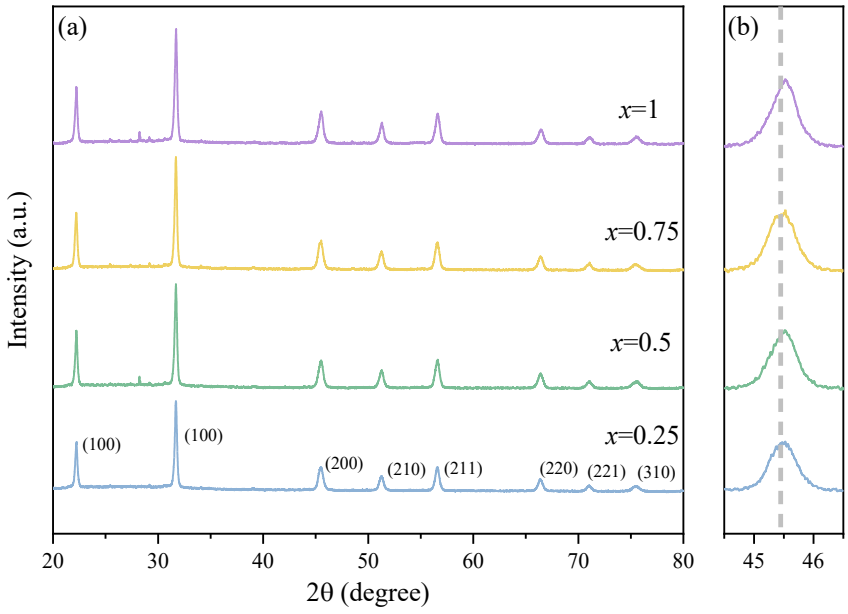


Fig. 1. (a) X-ray diffractometer (XRD) patterns of the *x*Dy–5Sr–KNN ceramics. (b) Magnified patterns at 2θ ranging from 44.5◦ to 46.5◦.

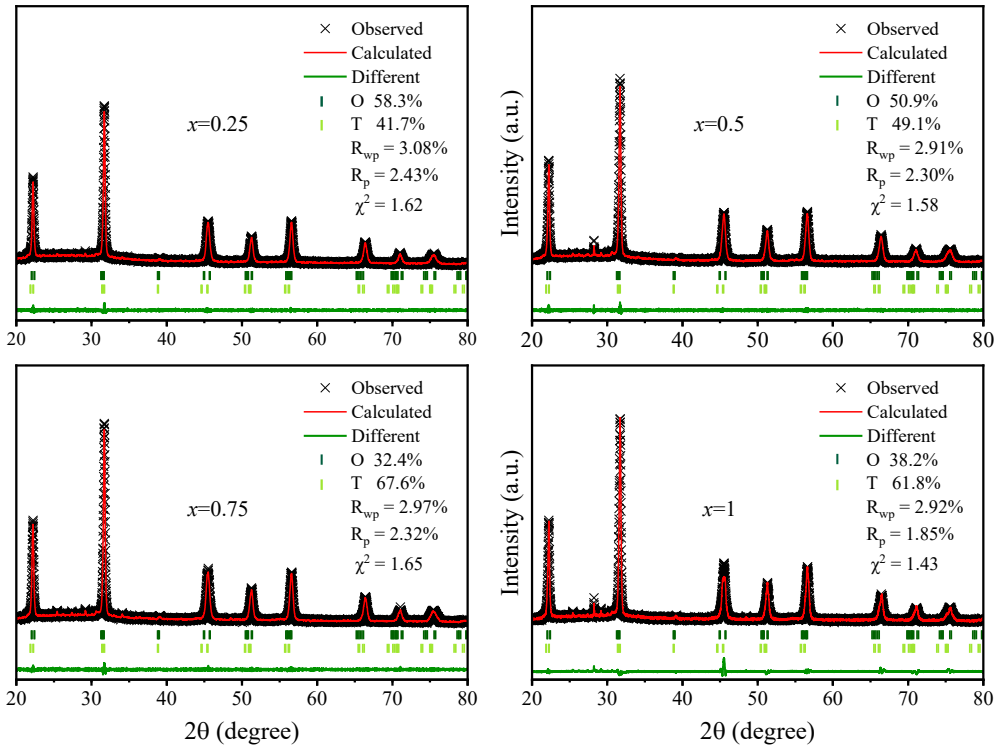


Fig. 2. (a-d) Processed XRD patterns of the *x*Dy-5Sr-KNN ceramics.

Fig. 1(a) displays the XRD patterns of *x*Dy-5Sr-KNN ceramics. All samples exhibited characteristic diffraction peaks of a perovskite structure. Given that Na^+ (CN=12, r=1.39 Å) and Sr^{2+} (1.44 Å) have comparable ionic radii, while both Dy^{3+} (1.03 Å) and Sr^{2+} are significantly smaller than K^+ (1.64 Å), Dy^{3+} and Sr^{2+} tended to occupy A-sites and preferentially substitute Na^+.[26] The lattice contraction occurred, and the diffraction peaks gradually shifted toward higher angles with the increasing Dy^{3+} content, as more clearly shown in the magnified view of Fig. 1(b).

To quantitatively evaluate the lattice structure, Rietveld refinement was performed on the diffraction data, as shown in Fig. 2(a-d). Compared with the typical orthorhombic phase of pure KNN, the co-doped ceramics exhibited markedly enhanced crystal symmetry. All samples showed a coexistence of orthorhombic (O) and tetragonal (T) phases, with the T phase fraction first increasing and then decreasing as the doping level increased. Notably, the x= 0.5 composition exhibits nearly balanced coexistence of the O and T phases. Such a nearly equal O/T phase proportion suggests strong competition between the two phases. Furthermore, the

previously reported temperature-dependent dielectric response of this system reveals two dielectric anomalies corresponding to the O–T and T–C phase transitions. The O–T dielectric anomaly exhibits a relatively broad peak and a composition-dependent variation of the transition temperature, while the frequency-dependent dielectric spectra reveal evident dielectric dispersion, indicating the diffuse characteristic of the O–T phase transition.[26] Considering both the structural refinement results and the reported dielectric behavior, the x= 0.5 composition can be reasonably described as exhibiting a nearly balanced O–T phase coexistence state. In contrast, the T-phase fraction reaches its maximum at x= 0.75, indicating a T-phase-dominated structure at this composition. Such enhanced structural symmetry establishes the structural prerequisite for understanding the composition-dependent optical and phonon behaviors presented below.

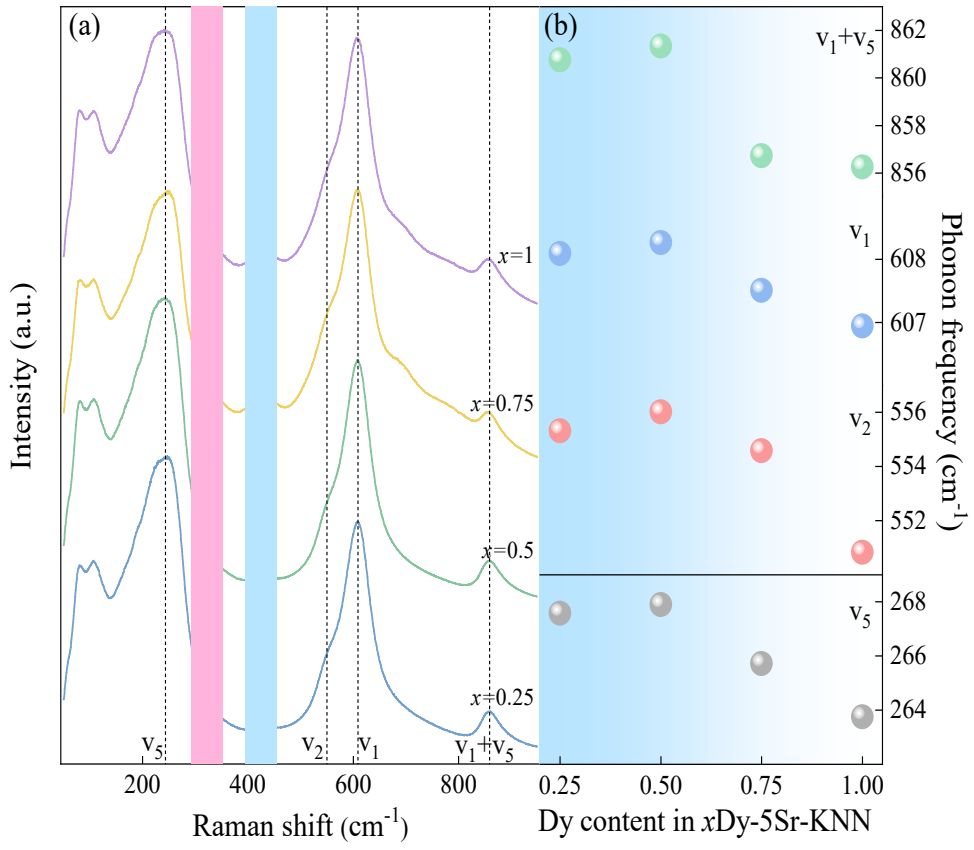


Fig. 3. (a) Raman spectra of the xDy-5Sr-KNN ceramics at room-temperature (b) The frequency variation of the dominant phonon modes with different Dy contents at room-temperature.

Combined with the room-temperature phase coexistence information quantified by XRD Rietveld refinement, Raman scattering was further used to characterize local lattice distortion and phonon evolution originating from A-site co-doping. Fig 3(a) illustrated the evolution of the Raman spectra with varying Dy^{3+} doping levels. According to point-group theory, the KNN lattice belongs to the space group Amm2, with predicted Raman-active optical modes of $4A_1+4B_1+3B_2+A_2$.[35,37] As a perovskite-derived material, the KNN lattice is built upon NbO_6 octahedra as the fundamental structural units. These NbO_6 octahedra exhibit multiple vibrational modes: the symmetric stretching mode $A_{1g}(\nu_1)$, the asymmetric stretching modes $E_g(\nu_2)$ and $F_{1u}(\nu_3)$, the asymmetric bending mode $F_{1u}(\nu_4)$, the symmetric bending mode $F_{2g}(\nu_5)$, and the Raman-inactive bending mode $F_{2u}(\nu_6)$. Experimentally, the Raman scattering intensities of the *x*Dy-5Sr-KNN ceramics were concentrated in three distinct regions. The region below 300 cm^{-1} corresponded to the symmetric bending mode (ν_5) and A-site cation vibrations. The 550–650 cm^{-1} region arose from the stretching modes (ν_1, ν_2, ν_3). The peak near 860 cm^{-1} is assigned to a combination band ($\nu_1 + \nu_5$). The asymmetric bending mode (ν_4) and inactive mode (ν_6) were not observed under the current experimental configuration. The Raman spectra evolve systematically with increasing Dy^{3+} concentration. The pink-shaded region below 300 cm^{-1} grew monotonically in intensity, reflecting progressive A-site Dy^{3+} incorporation and the associated low-frequency local vibrations. The blue shaded region in the 550–650 cm^{-1} range also intensified steadily, indicating continuous modification of the NbO_6 stretching vibrations. All characteristic peaks first shifted to higher wavenumbers and then to lower values as x increased, with the turning point at $x = 0.5$. The spectral linewidths reach a maximum at $x = 0.75$, indicating enhanced local lattice disorder and phonon scattering, which may contribute to the observed structural relaxation. This observation is consistent with the dielectric relaxation characteristics reported for this composition. The previously reported temperature-dependent dielectric response exhibits diffuse dielectric anomalies during the phase-transition process, and the dielectric maximum temperature (T_m) shows a frequency-dependent shift, indicating enhanced dielectric relaxation characteristics.

Furthermore, the modified Curie–Weiss analysis yields the highest diffuseness exponent (γ = 1.51) for x = 0.75 among the investigated compositions, suggesting a more diffuse transition and enhanced relaxor characteristics at this composition.[26]

To further explore the evolution of phonon modes, Raman-active phonon information was extracted via multi-Lorentzian peak fitting. Fig. 3(b) displayed the major phonon frequencies as a function of Dy^{3+} concentration. All vibrational modes exhibited a non-monotonic trend, with frequencies first increasing and then decreasing at x = 0.5. Given that the ionic radius of Dy^{3+} (1.03 Å) is substantially smaller than the average radius of A site K^+/Na^+ ions, A site substitution introduces local lattice contraction stress. When the Dy^{3+} doping level x is below 0.5, this stress shrinks the NbO_6 octahedra, shortens Nb-O bond lengths, and increases the bond force constant, thereby shifting phonon frequencies toward higher wavenumbers. The combined effects of chemical compression and local lattice strain become most pronounced at x = 0.5, leading to the most pronounced phonon hardening. The composition dependent variations in the refined Nb–O bond lengths further reveal the evolution of the local NbO_6 octahedral configuration, which may contribute to the observed changes in the Raman phonon frequencies.(Table S1) Specifically, the average Nb–O bond lengths decrease progressively with increasing Dy^{3+} concentration in both the T and O phases, indicating a gradual contraction of the local NbO_6 framework. Simultaneously, optimal matching of the O and T phase lattice parameters at this composition maximizes interfacial stress coupling, which further reinforces local confinement of phonon vibrations. In addition, the aliovalent substitution of Dy^{3+} for K^+/Na^+ modifies the local charge-compensation conditions and defect chemistry of the lattice. The resulting charge imbalance may be primarily accommodated through defect-compensation mechanisms involving A-site cation vacancies, while also affecting the oxygen vacancies associated with K/Na volatilization and high-temperature sintering. Consequently, the concentration and spatial distribution of oxygen vacancies may vary with the Dy^{3+} doping level, thereby influencing the degree of local lattice disorder and defect-mediated phonon scattering. Oxygen vacancies may also introduce defect-related electronic states that influence

optical absorption and provide non-radiative recombination pathways, potentially contributing to luminescence quenching. At an appropriate Dy^{3+} concentration, a more favorable defect configuration may alleviate excessive phonon scattering, thereby contributing to the maintenance of relatively high phonon frequencies. Therefore, the phonon hardening observed at low Dy^{3+} doping levels arises not only from the chemical compression induced by the smaller ionic radius of Dy^{3+}, but also from the synergistic effects of local lattice strain and defect-mediated lattice dynamics. When x exceeds 0.5, the T phase fraction continuously increases, lattice symmetry rises, and the c/a ratio approaches unity. The off centering of Nb^{5+} within the NbO_6 octahedron weakens, and the anisotropy of Nb–O bonds decreases. Concurrently, the disordered distribution of Dy^{3+} intensifies, which may promote extensive formation of PNRs. This process may disrupt long range ferroelectric order, allowing phonon softening dictated by relaxor disorder to become dominant, thus the phonon frequencies gradually decline. Notably, the peak phonon frequency occurs at $x = 0.5$, whereas the strongest relaxor characteristics appear at $x = 0.75$. This asynchrony reveals a complementary structural regulation mechanism in the Dy^{3+}/Sr^{2+} co-doped system. Specifically, $x = 0.5$ corresponds to the composition exhibiting the maximum phonon hardening, while $x = 0.75$ represents the optimized composition featuring enhanced long-range lattice symmetry and relaxor characteristics, consistent with the reported temperature-dependent dielectric response.[26] The evolution between these two compositions reflects a microscale physical transition from a phonon hardening regime governed by the combined effects of chemical compression and local lattice strain to a relaxor regime associated with enhanced lattice symmetry and disorder. Through Raman spectroscopy, a composition-driven structural transition from the O phase to the T phase is revealed.

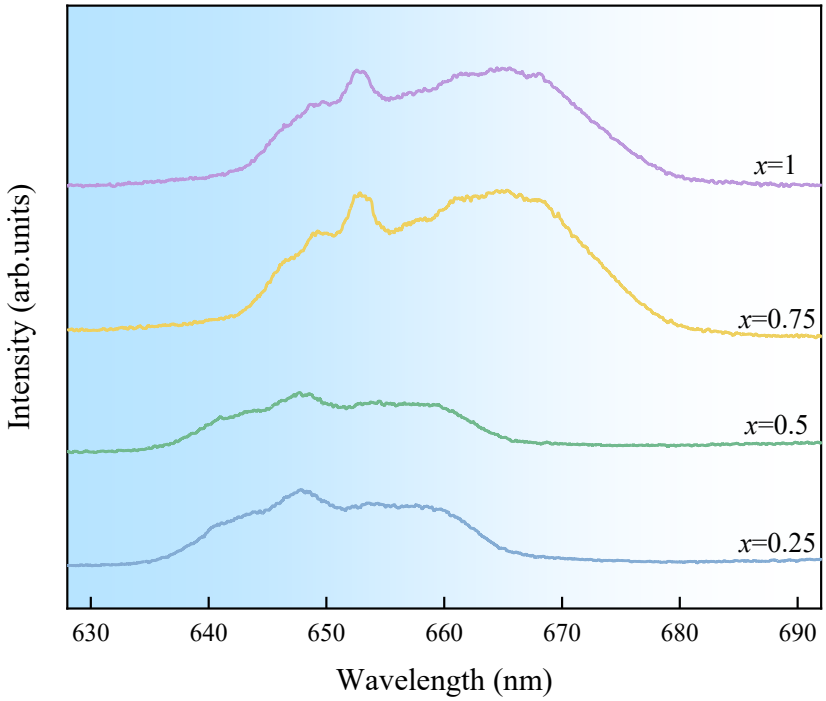


Fig. 4. Photoluminescence (PL) spectra of *x*Dy-5Sr-KNN at room-temperature.

The structural transformations evidenced by the Raman spectra naturally raise the question of how the concomitant lattice modifications influence the electronic states, which are the subjects of the following photoluminescence analysis. The room-temperature PL spectra of *x*Dy-5Sr-KNN ceramics with various Dy^{3+} doping levels were shown in Fig. 4. This emission band is assigned to the $^4F_{9/2}\rightarrow {}^6H_{11/2}$ transition of Dy^{3+} ions, corresponding to radiative recombination between distinct Stark sublevels.[38-41] A systematic redshift of the main emission peak was observed with increasing Dy^{3+} content, while the redshift is attributed to the significantly smaller ionic radius of Dy^{3+} (1.03 Å) compared with those of Na^+ (1.39 Å) and K^+ (1.64 Å). The incorporation of higher Dy^{3+} concentrations induces lattice contraction, leading to shortened Dy–O bond lengths and enhancing crystal field splitting. The reduced energy level spacings for the $^4F_{9/2}\rightarrow {}^6H_{11/2}$ transition result in a lowering of the emitted photon energy, and thus a shift of the peak toward longer wavelengths. It is noted that the redshift is not uniformly distributed across the whole composition range, where the most pronounced shift is concentrated in the interval between $x = 0.5$ and $x = 0.75$. This nonlinear evolution is tentatively ascribed not only to the cumulative lattice contraction effect but also to possible local structural

rearrangements that may occur within this intermediate composition region. Such structural modifications are suggested to further modulate the crystal field environment surrounding the Dy^{3+} sites, thereby amplifying the variation in energy level splitting across the x = 0.5–0.75 range. The PL intensity exhibited similar nonmonotonic composition dependence, while the intensities at x = 0.25 and 0.5 are comparably low but a marked enhancement is achieved at x = 0.75 and reaches the maximum. A slight reduction was observed at x= 1.0 compared with x = 0.75, yet it still substantially exceeds the levels at the two lower concentrations. Consistent with the phase-evolution results (Fig. 2), the T-phase fraction reaches its maximum at x = 0.75, resulting in a T-phase-dominated structure at this composition. The enhanced tetragonal phase fraction and the associated local structural characteristics may modify the crystal-field environment around the rare-earth ions, thereby contributing to the enhanced luminescence intensity. The emission intensity was synergistically enhanced by the increasing number of luminescent centers for $x < 0.75$, likely in conjunction with a growing fraction of the high symmetry tetragonal phase. The shortened average Dy^{3+}-Dy^{3+} distance activates nonradiative processes beyond this critical doping threshold, including resonant energy transfer and cross-relaxation via electric dipole-dipole interactions, which give rise to incipient concentration quenching.[41]

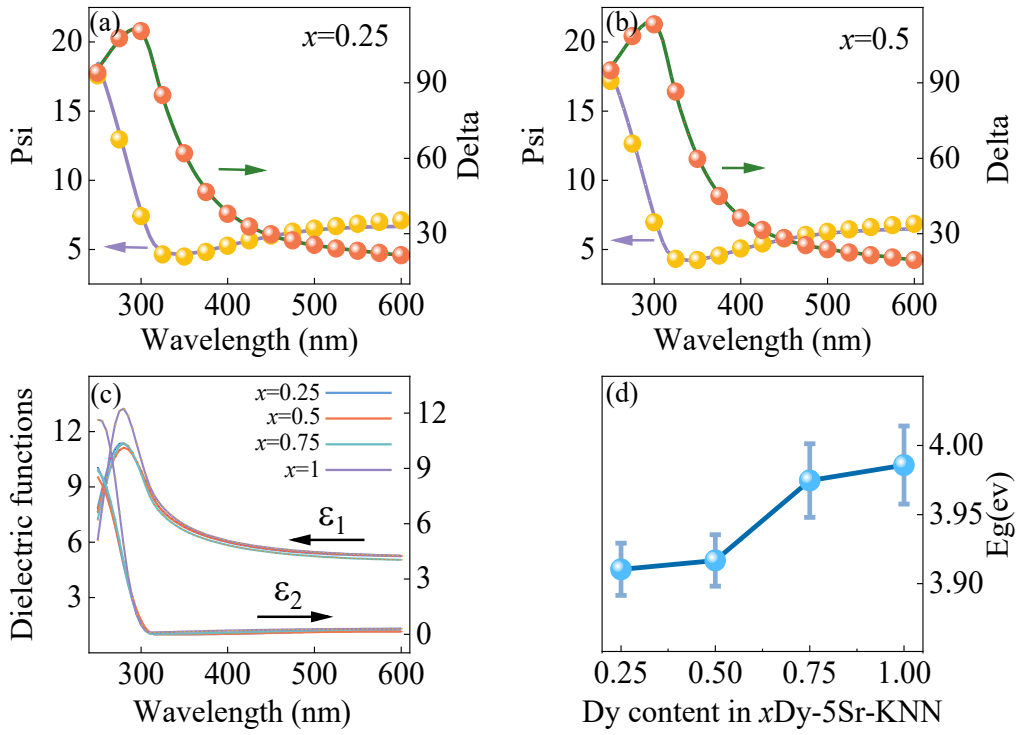


Fig. 5. The experimental (symbols) and modeled (solid curves) ellipsometric parameters (ψ, Δ) for (a) x = 0.25 and (b) x = 0.5 samples. (c) The dielectric functions (ε_1 and ε_2) of xDy-5Sr-KNN ceramic. (d) The optical bandgap as a function of the Dy content.

The luminescence differences arising from lattice distortion and O–T phase coexistence originate from modulated interband transitions. Accordingly, spectroscopic ellipsometry (SE) is employed to analyze the associated optical band characteristics, which provides fundamental clues to unravel the intrinsic electronic structure of xDy–5Sr–KNN ceramics. A triple-layer optical model with air, surface roughness layer and bulk xDy-5Sr-modified KNN layer was constructed to reconstruct the experimental spectral responses.[42] The roughness layer was parameterized via the Bruggeman effective medium approximation, assuming an equal volumetric occupancy of 50% air and 50% xDy-5Sr-KNN material. The dielectric response of the ceramic layer was modeled through a superimposed combination of Tauc-Lorentz and Gaussian oscillators. The resulting fitting curves plotted in Figs. 5(a) and 5(b) achieved excellent agreement with the experimental spectra, thus validating the accuracy of the adopted model. On the basis of the above

analysis, the real (ε_1) and imaginary (ε_2) components constituting the complex dielectric function of *x*Dy-5Sr-KNN ceramics were determined. It can be observed from Fig. 5(c) that ε_2 exhibited an extremely small magnitude below the fundamental absorption edge, which rules out the existence of extrinsic electronic transitions at low photon energies. The abrupt surge in ε_2 gave rise to prominent optical absorption with monotonically growing incident photon energy, which arose from interband electronic transitions across the valence band maximum and conduction band minimum. Meanwhile, ε_1 increased continuously with photon energy, reached its maximum near 4.5 eV, and declined thereafter as a consequence of Van Hove singularities.

The compositional evolution of the optical bandgap was quantitatively determined by extracting the bandgap energy (E_g) via the Tauc-Lorentz oscillator model. As plotted in Figure. 5(d), the optical band gap rose overall as the Dy molar fraction *x* increases from 0.25 to 1.0. A distinct sharp inflection point appeared in the range of x = 0.5-0.75, where the band gap increased steeply and deviates from simple monotonic doping behavior. This nonmonotonic jump matches well with the structural phase transition revealed by Raman and PL spectroscopy. In the vicinity of x=0.5, lattice compressive strain generated by Dy^{3+} substitution peaks, causing substantial stiffening of Nb-O bonds.[43] For x>0.5, the system underwent a gradual orthorhombic-to-tetragonal phase transition, accompanied by enhanced lattice symmetry. Simultaneously, excess electrons introduced by Dy^{3+} dopants may contribute to conduction band minimum via the Burstein-Moss effect. The joint contributions from abrupt alterations of the bonding configuration, electronic structure reconstruction, and amplified relaxor disorder gave rise to the anomalous bandgap widening across x = 0.5-0.75, which indicates that doping-induced structural phase transitions govern the evolution of the optical bandgap.

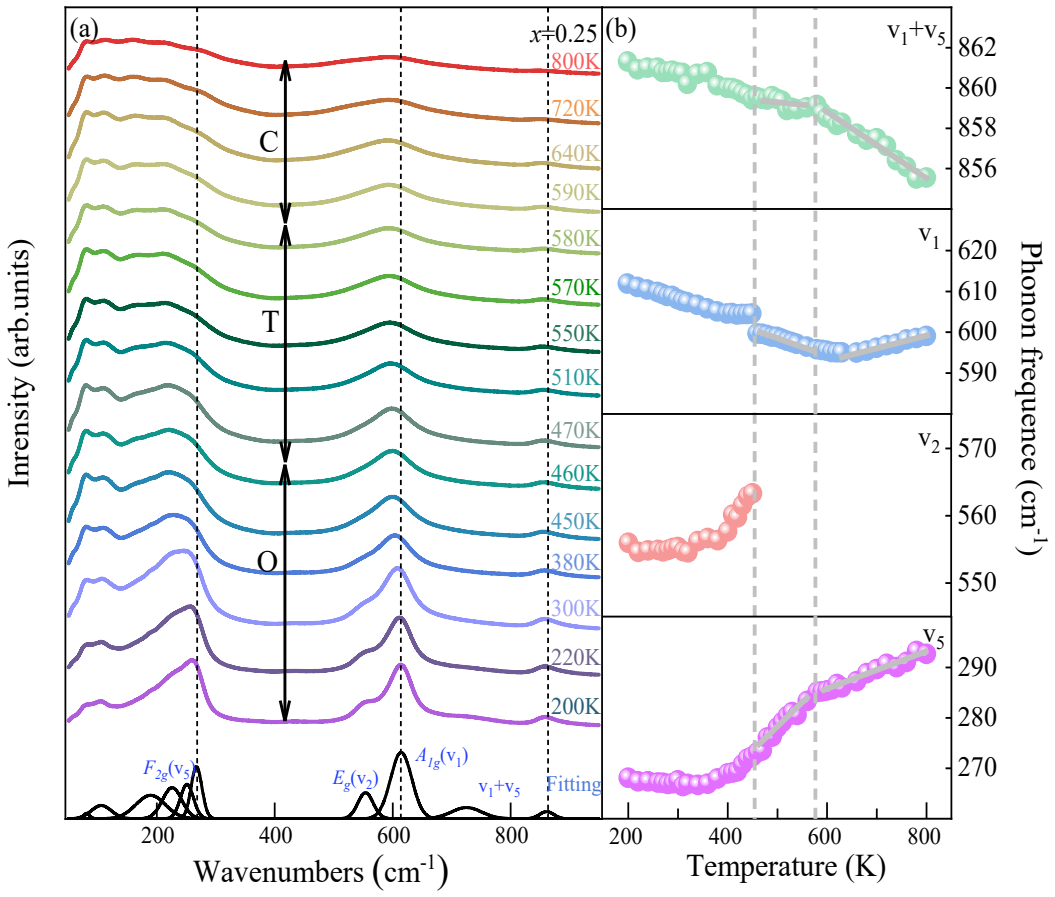


Fig. 6. (a) Temperature-dependent Raman spectra of *x*Dy-5Sr-KNN during heating from 200 to 800 K, while the details of fitting at 200 K are shown at the bottom. (b) The frequency variation of the main phonons for *x*Dy-5Sr-KNN ceramics with ascending temperature.

The above room-temperature characterizations systematically uncover the regulation rules of static lattice distortion, phase coexistence, optical band gap and luminescence by Dy^{3+}/Sr^{2+} co-doping. However, the phase evolution of ferroelectric perovskites is highly temperature-dependent. Therefore, variable-temperature spectroscopic tests are further performed to trace dynamic structural transitions and photoluminescence within a wide temperature range. To clarify the full picture of structural phase transition and lattice dynamics of KNN-based ceramics, we systematically characterized vibrational modes by temperature-dependent Raman spectroscopy from 200 to 800 K. Fig. 6(a) presents the temperature-dependent Raman spectra of the x = 0.25 KNN-based ceramic, which exhibited a clear evolution. As the

temperature rises, all characteristic peaks gradually broaden, weakened in intensity, and shift toward lower wavenumbers. This red shift and broadening trend persisted within the 200–580 K interval, accompanied by further peak widening. When the temperature exceeded 580 K, the intensity of the characteristic vibrational modes drops substantially, leaving only weak residual peaks superimposed on a broad background. This behavior was characteristic of the high-symmetry cubic phase, because the increased lattice symmetry induces degeneracy of all optical phonon modes and consequently leads to a marked reduction in Raman activity.

To elucidate the structural evolution mechanism, Lorentz multi-peak fitting was conducted for all collected Raman spectra. Temperature-dependent peak positions of main phonon modes were extracted from this fitting. The extracted fitting results are summarized in Fig. 6(b), which quantitatively illustrates phonon wavenumber shifts over distinct temperature ranges. An overall redshift of all phonon modes was observed with increasing temperature. The physical origin of these frequency shifts is now considered. Enhanced lattice thermal expansion and thermal disorder elongate the Nb–O bonds and reduce their force constants. Both effects contribute negatively to the phonon frequencies. Consequently, they account for the overall redshift observed with increasing temperature. Specifically, an anomalous frequency jump is exhibited by the ν_1 phonon when the temperature rose from 450 K to 460 K, and the ν_2 mode vanishes completely. A gradual blue shift was observed for the ν_5 mode, which only displays a subtle inflection in its hardening slope. These spectral features collectively testify to a structural transformation from the O to the T phase. The ν_1 phonon continued to soften upon entering the 470-580 K interval, meaning its frequency decreases with further heating. Meanwhile, the ν_5 mode underwent a steep monotonic hardening, while the $\nu_1+\nu_5$ combination mode exhibited a monotonic frequency decrease. Accordingly, this temperature region corresponds to the tetragonal phase. When the temperature exceeded 580–590 K, a distinct turning point is observed. The ν_1 phonon reversed its softening trend and began to harden, indicating a recovery of the effective force constant. The ν_5 mode maintained its hardening behavior but with a markedly reduced slope relative to the tetragonal phase.

The $\nu_1+\nu_5$ combination mode continued its monotonic decrease, and its slope also changes across this transition. Taken together, the spectral evolution across the three temperature regimes unequivocally confirmed a successive phase transition sequence. The KNN-based ceramic transformed from the orthorhombic phase through the tetragonal phase to the cubic phase. Except for slight differences in phase transition temperatures, all doped compositions exhibit identical temperature-dependent phonon evolution trends to the x = 0.25 sample. In addition, the temperature-dependent Raman spectra for all compositions have been provided in the Supporting Information, which further support the temperature-dependent structural evolution and phonon dynamics.

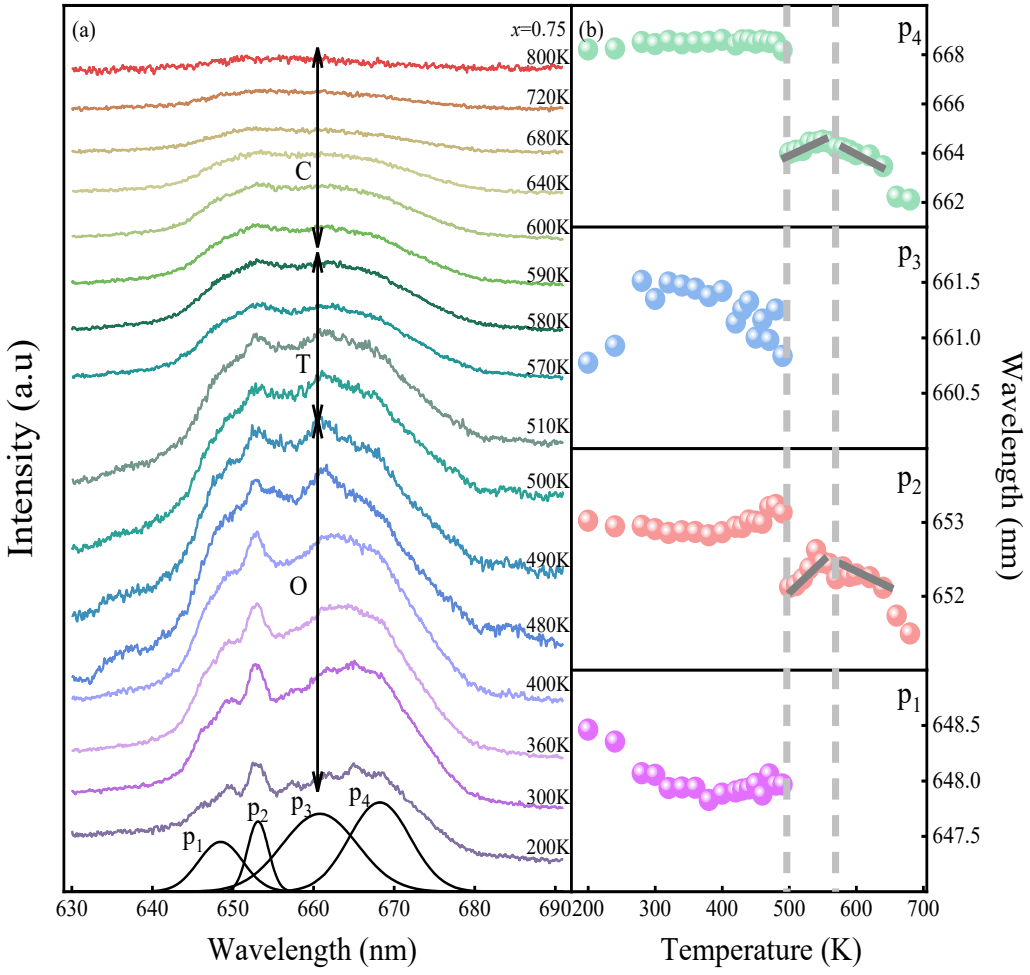


Fig. 7. (a)Temperature-dependent PL spectra of xDy-5Sr-KNN during heating from 200 to 800 K, while the details of fitting at 200 K are shown at the bottom. (b) The dominant PL peak wavelength for xDy-5Sr-KNN ceramics with ascending

temperature.

The temperature-dependent emission spectra of the KNN-based ceramic with a doping level of $x = 0.75$ were depicted in Fig. 7. These spectra serve as an effective probe for detecting structural transitions, owing to the high susceptibility of the features to the local crystal field environment. As illustrated in Fig. 7 (a), the spectral evolution with temperature can be delineated into three characteristic regimes based on the peak evolution behavior. The emission peaks were observed to broaden continuously and their intensities to diminish with rising temperature over the entire temperature range. This behavior was attributed to the enhanced nonradiative recombination arising from phonon-scattering processes, which became more efficacious at elevated temperatures. The PL spectra manifest pronounced multi peak splitting in the 200–490 K region, which reflects the Stark splitting of the Dy^{3+} energy levels induced by the low-symmetry crystal field of the orthorhombic structure.[44] A sudden spectral metamorphosis is observed upon traversing the first phase transition point at 490 K, while the original multi peak configuration progressively converts into two predominant peaks. This abrupt alteration was ascribed to the structural transformation from the orthorhombic to the tetragonal phase. Fig. 7(b) summarized the temperature trajectories of the peak positions derived from the spectral fitting. In the 490–590 K regime, the two principal peaks located at approximately 648 and 664 nm prevail, and both exhibited a gradual redshift with increasing temperature.[41] In contrast, both peaks shifted toward shorter wavelengths as temperature increased upon above 590 K. The change in the slope of the peak position versus temperature curves clearly evidenced the structural transition. The observed redshift in the tetragonal regime can be explained by lattice thermal expansion, where the expansion lengthens the Nb–O bonds. The crystal-field strength is thus monotonically attenuated as temperature rises, which narrows the energy gap between the $^4F_{9/2}$ and$^6H_{11/2}$ sublevels and reduces the energy of emitted photons. When the structure transition into the cubic phase, the Nb^{5+} ions reside at the centrosymmetric octahedral sites and the static off-center displacements disappeared. The high symmetry renders thermal vibrations the dominant perturbation source, while the vigorous thermal fluctuations

enhance the orbital overlap between the Dy^{3+} 4f electrons and the coordinating oxygen anions. The effective nuclear charge is augmented by the enhanced orbital overlap and the excited state centroid is elevated relative to the ground state by the electron phonon coupling. These combined effects yield higher emitted photon energies and a concomitant blueshift. Apart from minor discrepancies in phase transition temperatures, the x = 0.25 and x = 0.75 samples exhibit consistent temperature-dependent phonon evolution trends. The temperature-dependent PL spectra for all compositions have also been provided in the Supporting Information, offering additional information on the temperature-dependent optical response.

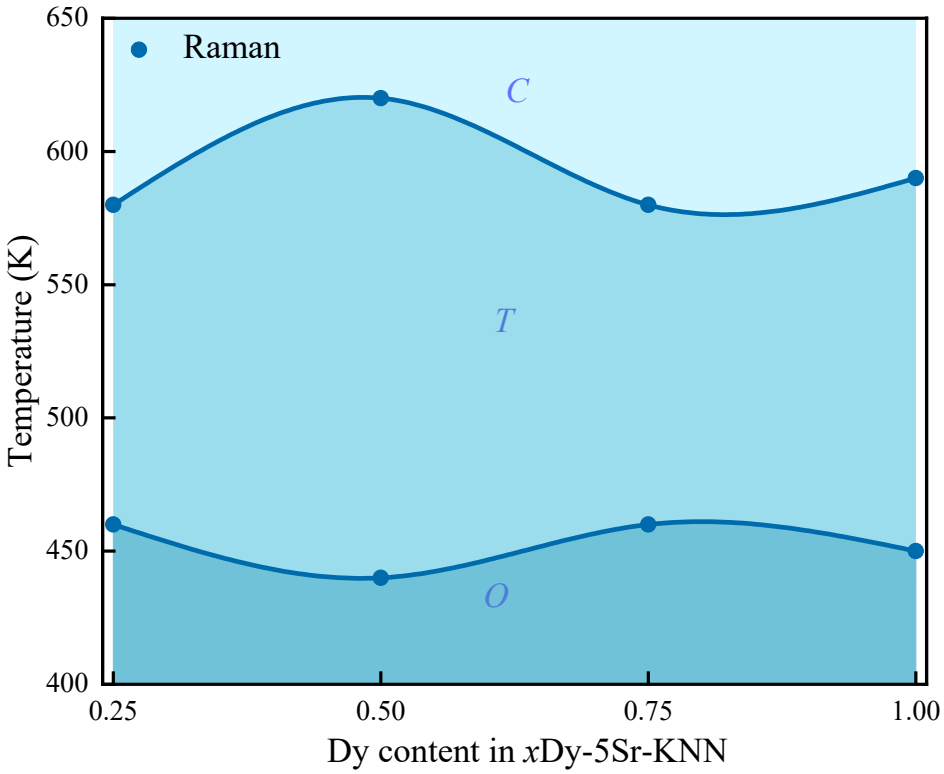


Fig. 8. Composition–temperature phase diagram for KNN-based ceramics with varying Dy contents.

A detailed composition-temperature phase diagram for the xDy-5Sr-KNN ceramic system was systematically constructed based on a comprehensive integration of variable-temperature Raman spectra as presented in Fig. 8. The O–T phase transition temperature exhibited a non-monotonic dependence on composition, accompanied by a corresponding variation in the room-temperature T-phase fraction. Notably, although

the x = 0.75 composition manifests the highest T-phase proportion under ambient conditions, its O–T transition temperature was marginally elevated relative to that of the x = 0.5 sample. This seemingly anomalous phenomenon can be attributed to the competing influence of Dy^{3+}/Sr^{2+} co-doping on the lattice thermodynamic stability and the kinetic pathways of the phase transformation. The established phase diagram not only delineates the thermodynamically stable regimes of the xDy–5Sr–KNN system, but also offers a strategic framework for precisely tailoring the phase boundary via compositional engineering.

In summary, the composition-temperature phase evolution in Dy^{3+}/Sr^{2+} co-doped KNN-based ceramics has been systematically elucidated. The O–T phase coexistence with the maximum tetragonal phase fraction at x=0.75 was verified at room temperature. Asynchronous Nb–O bond stiffening and optimal relaxor ferroelectric features were uncovered across doping gradients, together with anomalous bandgap broadening and redshifted, intensified luminescence centered at x=0.75, which collectively suggests that structural modification proved to dominate both electronic transitions and luminescence responses. The successive O–T–C phase transitions were unequivocally identified based on lattice dynamical and luminescence spectroscopic analyses across the entire temperature range, while the structural transitions verified to modulate local crystal-field surroundings and electron phonon coupling, generating characteristic phonon frequency anomalies and reversible luminescence shift trends. These findings provide a critical foundation for the compositional design and performance optimization of KNN-based ferroelectric systems, offering a viable pathway toward thermally stable lead-free optoelectronic materials.

References

[1] Wu J 2020 *J. Appl. Phys.* **127** 190901

[2] Zheng T, Wu H, Yuan Y, Lv X, Li Q, Men T, Zhao C, Xiao D, Wu J, Wang K, Li J F, Gu Y, Zhu J and Pennycook S J 2017 *Energy Environ. Sci.* **10** 528

[3] Xu K, Li J, Lv X, Wu J, Zhang X, Xiao D and Zhu J 2016 *Adv. Mater.* **28** 8519

[4] Wu Y, Soon P, Lu J, Zhou J, Liu Y, Guo Z, Wang K and Gong W 2024 *EcoMat* **6** e12450

[5] Tian S, Zhao Z, Li B and Dai Y 2026 *Microstructures* **6** 2026002

[6] Wu Q, Zhang F, Wang B, Cheng Z, Liu S, Zhu R, Huang Y, Chang J, Liu Z and Dong S 2025 *J. Materiomics* **11** 100876
[7] Liu H, Hao Y, Yang Z, Feng T, Su B, Zhang X, Xue M, Zhang B P and Li J F 2024 *J. Adv. Ceram.* **13** 364
[8] Lin J, Ge G, Li J, Qian J, Zhu K, Wei Y, Shi C, Li G, Yan F, Li W, Zhang J, Zhai J and Wu H 2023 *Adv. Funct. Mater.* **33** 2303965
[9] Yang B, Peng H, Zhang Y, Shang X, Zhou T and Guo J 2023 *Mater. Res. Bull.* **158** 112077
[10] Poonam, Sinha N, Yadav T, Ojha P K, Verma V and Kumar B 2026 *J. Mater. Sci.: Mater. Electron.* **37** 1497
[11] Huang H, Zheng T and Wu J 2024 *Inorg. Chem.* **63** 22549
[12] Duan L, Wei Y, Xu T, Zhang A, Zhang Y, Xu Z and Chu R 2024 *J. Adv. Dielect.* **15** 24400186
[13] Sun Q, Yuan C, Liu X, Zhang X, Zhao J, Zhou C, Rao G, Su K and Wang D 2024 *New J. Chem*. **48** 5495
[14] Hino K, Morikawa D, Fu D, Itoh M and Tsuda K 2026 arXiv:2607.13364 [cond-mat.mtrl-sci]
[15] Lin J, Ge G, Zhu K, Bai H, Sa B, Yan F, Li G, Shi C, Zhai J, Wu X and Zhang Q 2022 *Chem. Eng. J.* **444** 136538
[16] Wang X, Lv X, Ma Y, Zhang X, Lyu J and Wu J 2023 *Acta Mater.* **254** 118997
[17] Lin Q, Shen J, Zeng X, Huang X, Shi W, Sa B, Yan H, Gao M, Zhao C, Lin C, Wu X, Lin J and Zhai J 2026 *ACS Nano* **20** 17803
[18] Liu J, Zha J, Yang Y, Lu X, Hu X, Yan S, Wu Z and Huang F 2024 *Chin. Phys. Lett.* **41** 077701
[19] Wu L, Tan Z, Zheng T and Wu J 2023 *J. Am. Ceram. Soc.* **106** 6664
[20] Wang N, Shi S, Ye J, Bi Z, Qiu W, Xu J, Yang L and Wang H 2024 *J. Mater. Sci.: Mater. Electron.* **35** 1921
[21] Chauhan A, Verma R, Krishnan C G, Jayavel R, Batoo K M, Hussain S, Kumar R and Kumar P 2023 *Appl. Phys. A* **129** 117
[22] Zhou P, Lin Q, Zeng X, Gao M, Zhao C, Lin C, Lin T and Wu X 2025 *J. Rare Earths* **43** 2479
[23] Wu X, Wang P, Jiang X, Cao S, Lin J, Xiong R, Zheng Z, Gao M, Zhao C, Lin T, Lin C and Sa B 2024 *ACS Appl. Mater. Interfaces* **16** 55760
[24] Yu F, Ma B, Xie Z, Wang P, Wu X, Lin C, Zhao C, Gao M, Luo L and Zhang Q 2023 *J. Eur. Ceram. Soc.* **43** 4408
[25] Xin R, Wang Y, Fang Z, Zheng F, Gao W, Fu D, Shi G, Liu J-Y and Zhang Y 2024 *Chin. Phys. B* **33** 087701
[26] Huang H, Zhang S, Yu F, Lin J, Wu X, Zhao C, Gao M, Lin T, Jin Y and Lin C 2024 *J. Am. Ceram. Soc.* **107** 1137
[27] Tao H, Wu H, Liu Y, Zhang Y, Wu J, Li F, Lyu X, Zhao C, Xiao D, Zhu J and Pennycook S J 2019 *J. Am. Chem. Soc.* **141** 13987
[28] Zheng T, Wu J, Xiao D and Zhu J 2018 *Prog. Mater. Sci.* **98** 552
[29] Huang Y, Wang X, Ma Y, Lv X and Wu J 2023 *J. Am. Ceram. Soc.* **107** 355
[30] Li R, Sun X, Lv X, Zheng T and Wu J 2021 *Acta Mater.* **218** 117229

[31] Zou J, Hao S, Gemeiner P, Guiblin N, Ibder O, Dkhil B and Paillard C 2024 *J. Mater. Chem. C* **12** 600
[32] Zhang Y, Feng X, Li F, Meng D, Zheng T and Wu J 2023 *Adv. Funct. Mater.* **33** 2306039
[33] Qi X, Ren P, Tong X, Wang X and Zhuo F 2025 *J. Eur. Ceram. Soc.* **45** 116874
[34] Wang L G, Wang Y S, Zhu C M, Qin M Y, Wei J Y and Jiang Y 2024 *Phys. Chem. Chem. Phys.* **26** 7083
[35] Saha M, Niranjan M K and Asthana S 2024 *J. Phys.: Condens. Matter* **36** 425703
[36] Buixaderas E, Gregora I, Hlinka J, Dec J and Lukasiewicz T 2013 *Phase Transit.* **86** 217
[37] Li Y, Cui A, Dai K, Yan Y, Jiang K, Shang L, Zhu L, Li Y, Zhang J, Lv X, Wu J and Hu Z 2024 *Acta Mater.* **265** 119612
[38] Arunkumar S, Venkataiah G and Marimuthu K 2015 *Spectrochim. Acta A* **136** 1684
[39] Chepyga L M, Hertle E, Aissaoui A, Zigan L, Osvet A, Brabec C J and Batentschuk M 2018 *J. Lumin.* **197** 23
[40] Naseer K A, Sathiyapriya G, Marimuthu K and Piotrowski T 2022 *Optik* **251** 168436
[41] Pawar P P, Munishwar S R, Gautam S and Gedam R S 2017 *J. Lumin*. **182** 65
[42] Zou J, Wei T, Song M, Zeng S, Zhou K, Zhang Y, Zhang S and Zhang D 2025 *Adv. Funct. Mater.* **35** 2425080
[43] Ding Y, Tan Z, Pan Y, Wang Y, Dong Y, Liu W, Zheng T and Wu J 2025 *Small* **21** 2502418
[44] Lin C, Wang H, Wang P, Wu X, Lin T, Sa B, Cheng Y, Zheng X, Yu X and Fang C 2021 *J. Am. Ceram. Soc.* **104** 903

Funding

This study was funded by the National Natural Science Foundation of China (Grant No. 12504018 and Grant No. U2141240), the Shanghai Sailing Program (Grant No. 24YF2745000), the Chenguang Program of Shanghai Education Development Foundation and Shanghai Municipal Education Commission.